Simple Synthesis of Mesoporous Carbon Nanofibers with Hierarchical Nanostructure for Ultrahigh Lithium Storage

Yalan Xing,[†,‡] Yanjie Wang,[‡] Chungen Zhou,[†] Shichao Zhang,*[,†] and Baizeng Fang*[,‡]

[†]School of Materials Science and Engineering, Beihang University, 37 Xueyuan Road, Beijing 100191, People's Republic of China

[‡]Department of Chemical & Biological Engineering, University of British Columbia, 2360 East Mall, Vancouver, British Columbia, Canada V6T 1Z3

Ⓢ *Supporting Information*

ABSTRACT: In this study, a simple and reproducible synthesis strategy was developed to fabricate mesoporous carbon nanofibers (MCNFs) by using dual hard templates, a porous anodic aluminum oxide (AAO) membrane, and colloidal silica (Ludox TM-40). By using commercial templates, and removing AAO and the silica simultaneously, the synthesis procedures for MCNFs are greatly simplified without the need for separate preparation or the removal of templates in sequence. With phenol resin as a carbon precursor, the as-prepared MCNFs material reveals not only high surface area and mesoporous volume but also hierarchical nanostructure composed of hollow macrochannels derived from the AAO template, large mesopores (ca. 22 nm) from the removal of silica particles and micropores from the carbonization of phenol resin. Such unique surface and structural characteristics could provide a large quantity of active sites for Li storage and facilitate fast mass transport. Moreover, a one-dimensional (1D) carbon nanofiber (CNF) nanostructure favors fast electron transfer. The as-prepared MCNF anode demonstrates ultrahigh lithium storage capacity particularly at high rates, which is much higher than that reported for the commercial graphite and also significantly higher than other nanostructured carbon materials, such as ordered mesoporous carbon CMK-3 and ordered multimodal porous carbon (OMPC).

KEYWORDS: mesoporous carbon nanofibers, template method, hierarchical porosity, nanostructured carbon, lithium storage
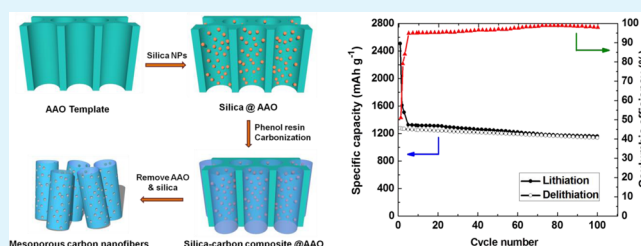
1. INTRODUCTION

Electrochemical energy storage has become a critical technology for a variety of applications, including smart grids, electric vehicles, and portable electronic devices. The lithium-ion battery (LIB) is currently the most attractive energy storage device, because of its relatively high energy density and long cycle life.[1−7] However, higher demand for both energy density and power density in versatile applications is still a challenge for LIB. Hence, great efforts have been devoted to explore novel electrode materials with higher capacity, better rate performance, and lower cost.

Graphite, the most commonly used anode material in today's commercial rechargeable LIBs, has advantages in low cost, low electrochemical potential (with respect to lithium metal), and good cyclic stability.[8] However, the limited intercalation capacity (with a theoretical capacity of 372 mAh/g) and poor rate performance have hindered its application.[9] As an alternative to carbon-based anode, some metal or metal oxides (such as tin,[10] SnO2,[11,12] antimony,[13] and silicon[14−18]) are widely studied, since they could alloy with lithium and show much higher specific capacity, but severe capacity loss during cycling is still a problem for practical usage. Therefore, improvements based on carbonaceous anode materials are attractive ways to enhance the electrochemical performance of anode in LIB. Several strategies have been developed including

fabricating a three-dimensional (3D) multifunctional architecture and introducing mesopores into these frameworks.[19,20]

Bulk carbonaceous materials suffer from slow lithium diffusion rates within their frameworks, thus limiting their rate capabilities.[10] A 3D carbon architecture will generate a well-interconnected wall structure, providing a continuous electron pathway and thus yield fast electron transport. While mesoporous characteristic will favor higher electrode/electrolyte contact area, shorter path lengths for electron and Li+ transport, and better accommodation of the strain of Li+ insertion/removal.[21] Consequently, 3D structured porous electrode materials have higher capacities and much faster rate performance than their corresponding bulk counterparts.[10]

Nanofibers, as an important type of carbon structure, could form a 3D aligned architecture that provides good conductive network for electron transfer. One simple and practical way to prepare nanofibers is to employ a hard template with well-ordered regular channels, such as anodic aluminum oxide (AAO) membranes,[22] through which many materials including well-ordered arrays of mesoporous silica nanowires and titania nanotubes have been prepared.[23−26] Although so, little research

about mesoporous carbon nanofibers (MCNFs) fabricated through AAO template has been reported. Herein, we target our research at introducing mesopores into carbon nanofibers (CNFs) by using AAO and commercially available colloidal silica as co-templates and phenol resin as a carbon precursor.

Compared with other reports, which may involve separate preparation of a carbon precursor,[27,28] or separate preparation of colloidal silica and separate removal of templates,[29] or a variety of surfactants as structure directing agents,[22] our method reported in this study, using commercial colloidal silica Ludox TM-40 as a co-template and removing AAO and the silica simultaneously by NaOH, is much simpler and more efficient to fabricate MCNFs. In addition, by using silica nanoparticles (NPs) as a co-template the mesopores size could be easily tailored by adjusting the size of silica NPs template. Compared with the MCNFs prepared by other approaches, the as-prepared MCNFs material has much larger mesoporous size, which facilitates fast mass transport at high charge−discharge rates. Because of its superior surface and structural character-istics, that is, large active surface area and mesoporous volume for high Li storage, and the hierarchical porosity composed of macroscaled channels of CNFs and mesopore arrays along the wall of CNFs which favor fast mass transport, and 1D CNF nanostructure favors fast electron transfer, the as-prepared MCNFs anode reveals much higher lithium storage capacity than its counterparts, such as commercial graphite, ordered mesoporous carbon CMK-3, and ordered multimodal porous carbon (OMPC).

2. EXPERIMENTAL SECTION

2.1. Synthesis of MCNFs. Colloidal silica Ludox TM-40 particles 20−30 nm in size were used as a porogen of AAO-templated CNF. For a typical synthesis, colloidal silica Ludox TM-40 NPs (Sigma−Aldrich, 40 wt % colloidal silica in water) were incorporated into the interior walls of AAO membrane (Whatman Anodisc 25, ca. 200−300 nm in channel diameter) through the infiltration. After drying at 353 K overnight, 0.187 g of phenol and 0.169 g of paraformaldehyde were introduced followed by a heating treatment at 403 K under vacuum for 12 h to generate phenol resin incorporated silica−AAO composite. After carbonization at 973 K under N_2 gas flow for 3 h to convert the polymer into carbon, the AAO membrane and silica particles were then simultaneously removed using 2 M NaOH solution at 353 K. The data obtained from thermogravimetric analysis (as shown in Figure S1 in the Supporting Information) suggests that the residue remains ca. 5.4 wt % in the as-prepared MCNFs sample.

OMPC and CMK-3 reported previously for LIB application were chosen for the comparison of Li storage capacity in porous carbon materials with different nanostructures. OMPC was prepared by using bimodal porous silica (BPS), which was fabricated through a self-assembly of polystylene and colloidal silica NPs, as a sacrificial template and furfuryl alcohol (FFA) as the carbon precursor. Ordered mesoporous carbon CMK-3 was fabricated by a replication through nanocasting of SBA-15 silica, and using FFA as the carbon source. Details on the preparation of BPS, OMPC, and CMK-3 can be seen in a previous report.[6]

2.2. Surface and Structural Characterization. N_2 adsorption and desorption isotherms were measured at 77 K on a Micromeritics ASAP-2020 gas adsorption analyzer after a sample was degassed at 423 K to 20 mTorr for 12 h. The specific surface areas were determined from nitrogen adsorption using the Brunauer−Emmett−Teller (BET) meth-

od. Total pore volumes (V_{total}) were determined from the amount of gas adsorbed at a relative pressure of 0.99. Micropore size (pore size <2 nm) and volume (V_{micro}) were calculated from the analysis of the adsorption isotherms using the Horvath−Kawazoe (HK) method. Pore size distribution (PSD) was calculated from the analysis of the adsorption branch, using the Barrett−Joyner−Halenda (BJH) method.

Surface morphology of the as-prepared MCNFs was examined via scanning electron microscopy (SEM) (FEI Helios, Model NanoLab 650 FIB SEM) or by a Cameca Model SX-50 scanning electron microprobe with four vertical wavelength-dispersion X-ray spectrometers and a fully-integrated SAMx energy-dispersion X-ray spectrometer.

High-resolution transmission electron microscopy (HRTEM) images were obtained on a JEOL Model FE-2010 microscope operated at 200 kV.

X-ray diffraction (XRD) patterns were obtained on a Bruker D8 Focus (LynxEye detector) powder X-ray diffractometers using Co Kα radiation as the X-ray source, operating at 35 kV and 40 mA. The diffractograms were recorded in the 2θ range 10°−80°, in steps of 0.02° with a count time of 20 s at each point.

2.3. Electrochemical Test Cells Setup. For LIB perform-ance tests, a three-electrode cell was constructed, in which metallic lithium sheets were used as the counter and reference electrodes and the as-prepared MCNFs as the working electrode. A typical fabrication of the working electrode is as follows. The as-synthesized MCNFs powder (active material, 90 wt %) was ground with polytetrafluoroethylene (binder, 10 wt %) to make a paste, which was then pressed on a copper mesh (current collector). The as-prepared electrode was dried under vacuum at 393 K overnight prior to use.

1 M $LiClO_4$−EC−DEC (where EC is ethylene carbonate and DEC is diethyl carbonate; the EC:DEC volume ratio equals 1) was used as the electrolyte. Electrochemical cells were constructed in a glove box under an inert atmosphere.

2.4. Electrochemical Characterization. Various electro-chemical techniques such as constant current charge−discharge measurements and electrochemical impedance spectroscopy (EIS) were utilized to characterize the MCNFs anode in LIBs. Constant current charge−discharge tests were performed with the cut-off voltage limits of 0.005 and 3.0 V. EIS measurements were conducted after 100 charge−discharge cycles at a rate of 100 mA g^{-1} in the frequency range of 100 kHz to 0.01 Hz with a zero-bias potential and 10 mV of amplitude. Impedance spectrum was analyzed by fitting the spectrum to the proposed equivalent circuit, using Zview software.

3. RESULTS AND DISCUSSION

3.1. Surface and Structural Characteristics of MCNFs. MCNFs were fabricated through a simple but reproducible nanocasting technology by using commercially available porous AAO membrane as a hard template and colloidal silica Ludox TM-40 as a co-template, and phenol resin as a carbon source, as shown in Figure 1A. Colloidal silica NPs were firstly incorporated into the interior walls of AAO membrane to form a uniform layer of the silica NPs, as revealed by the SEM image shown in Figure 1B. After drying overnight at 353 K, the incorporated silica NPs could attach firmly to the interior walls of AAO probably due to a strong interaction between the silica and AAO substrate. After the introduction of phenol resin into the dual templates and carbonization at 973 K under N_2 gas flow, the polymer turned into carbon, forming a layer covering
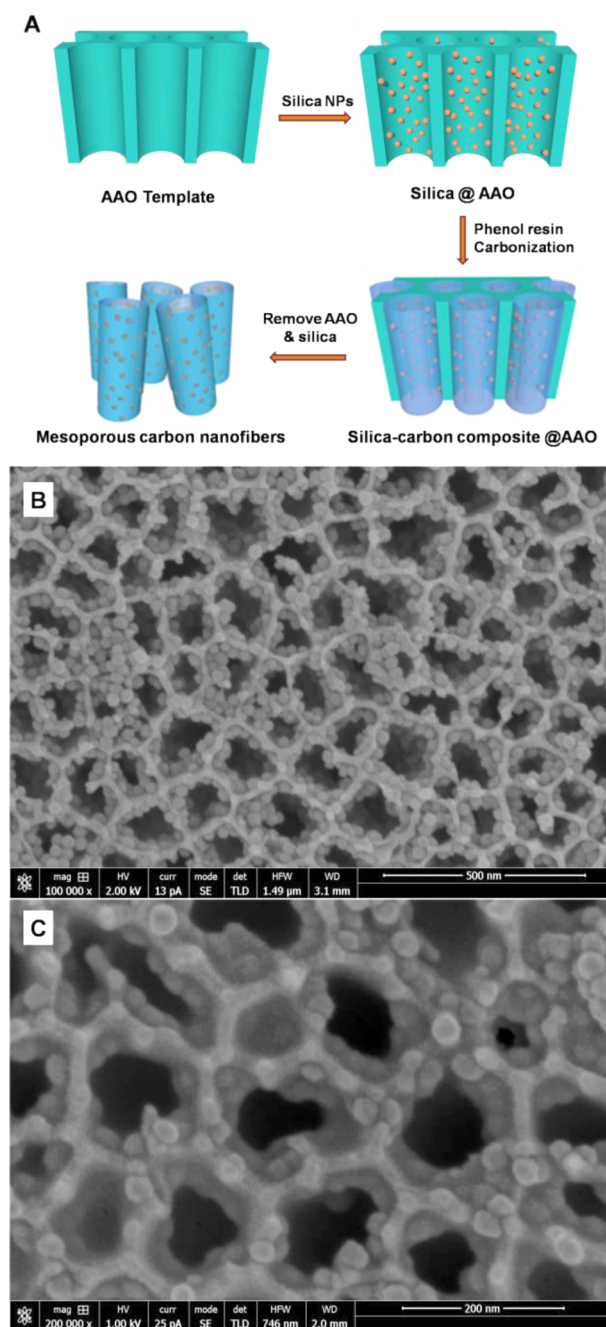
Figure 1. Schematic diagram for the synthesis of (A) MCNFs (AAO = anodic aluminum oxide, NPs = nanoparticles) and SEM images for (B) silica@AAO and (C) silica–carbon@AAO.

the silica NPs, as shown in Figure 1C. The obtained silica-carbon composite@AAO was etched in the alkaline solution to remove AAO and silica NPs simultaneously, thus generating free-standing MCNFs.

Figure 2 shows representative SEM images for the as-prepared MCNFs. As shown in Figure 2A, the as-prepared MCNFs sample has a length of ca. 40 μm, which corresponds well to the channel length of the AAO membrane. From Figure 2B, it is clear that the CNFs are separate and discrete, and almost uniform in fiber diameter. In addition, it is noteworthy that, from the intersection of some broken fibers in Figures 2A and 2B, hollow channels of ca. 100 nm in diameter were clearly observed. Whether a hollow channel will be developed or not
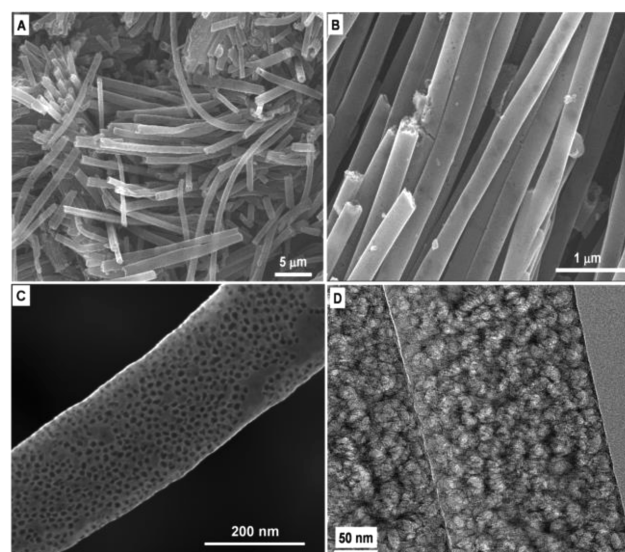
Figure 2. (A–C) Representative SEM images for the as-prepared MCNFs with various magnifications (panels A and B show low magnifications, while panel C shows high magnification), and (D) HRTEM image for the MCNFs.

depends highly on the amount of silica NPs and the quantity of phenolic resin incorporated into the AAO channels, as seen from Figures 1B and 1C. If an AAO channel is fully occupied by the silica NPs, after the filling of phenolic resin and the carbonization, a CNF will be developed without a hollow channel. In this study, appropriate amounts of silica NPs and phenolic resin were incorporated into the AAO channels, resulting in hollow channels developed for the as-prepared MCNFs in most cases. The SEM image with high magnification in Figure 2C and HRTEM image in Figure 2D further reveal that the as-prepared single MCNF has a diameter of ca. 220–240 nm with uniform open mesopore (ca. 10–25 nm) arrays on the wall. The STEM images shown in Figure S2 in the Supporting Information also confirm the uniform distribution of mesopores on the walls of the CNFs.

A representative XRD pattern is shown in Figure 3 for the as-obtained MCNFs. The pattern reveals a strong diffraction peak located at ca. 27.9° and a weak peak at 49.7°. Moreover, no other diffraction peaks are clearly observed. These diffraction lines correspond to the 002 and 101 reflections of graphite, respectively. In addition, the XRD pattern reveals an
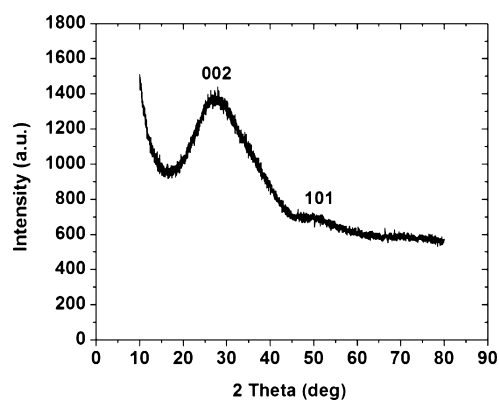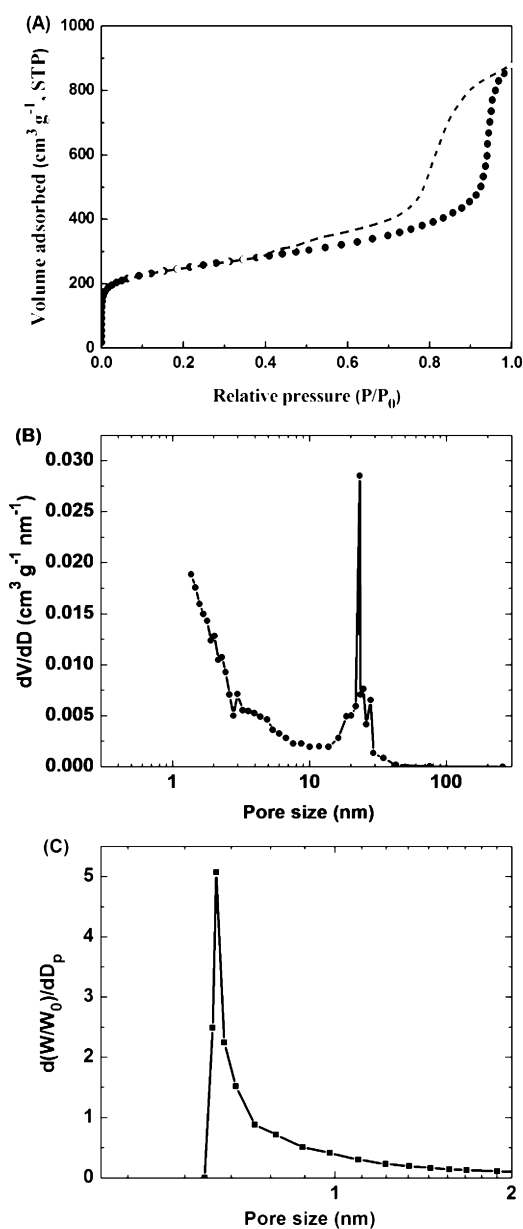

Figure 3. Representative XRD pattern for the as-prepared MCNFs.

amorphous structure that can be considered to be a partly graphitized carbon.[28]

Nitrogen adsorption−desorption isotherms shown in Figure 4A reveal a Type IV isotherm with H3 hysteresis, according to

Figure 4. (A) Nitrogen adsorption−desorption isotherms at 77 K, (B) the derived pore size distribution from the Barrett−Joyner−Halenda (BJH) method, and (C) the micropore size distribution derived from the Horvath−Kawazoe method for the as-prepared MCNFs.

the IUPAC classification, corresponding to framework mesopores. The particle size distribution (PSD) plot in Figure 4B shows a mean mesopore size of ca. 22 nm, which is slightly smaller than that (ca. 20−30 nm) of the silica NPs template, caused by the shrinkage of polymer and silica during carbonization. The BET measurement also reveals the as-prepared MCNFs sample has a BET surface area of ca. 872 m^2 g^{-1}, mesoporous volume of 1.28 cm^3 g^{-1}, and microporous volume of 0.34 cm^3 g^{-1}. The mean micropore size derived from the HK method is ca. 0.65 nm, as shown in Figure 4C. These micropores were also generated by the shrinkage of phenol

resin during carbonization. Table 1 summarizes the BET data obtained for the as-prepared MCNFs and some data reported previously for other nanostructured materials CMK-3 and OMPC.[6]

Table 1. Structural Parameters Derived from the N$_2$ Adsorption−Desorption Isotherms Obtained at 77 K for the As-Prepared MCNFs[a]

sample	specific surface area, S_{BET} (m^2/g)	micropore volume, V_{micro} (cm^3/g)	mesopore volume, V_{meso} (cm^3/g)	pore size distribution, PSD (nm)
MCNF	872	0.34	1.28	22
CMK-3	1228	0.56	1.21	3.9
OMPC	1120	0.24	2.12	23

[a]Other nanostructured materials CMK-3 and OMPC reported for LIB application[6] are also listed here for comparison.

From the SEM images and BET measurement, it is evident that the MCNF carbon material has not only a large surface area but also a hierarchical porosity composed of macro-channels (ca. 100 nm) derived from the AAO template, large mesopores (pore size: ca. 22 nm) generated from the removal of colloidal silica particles, and micropores (mean pore size: ca. 0.65 nm) produced from the carbonization of phenol resin.

3.2. Lithium Storage in Various Porous Carbon Materials. Compared with the MCNFs produced by other researchers, the as-prepared MCNFs developed in our study not only have high specific surface area, but also much larger mesopore (ca. 22 nm in size) connected to open macroporous channel and micropores. Such 3D porous architecture is expected to exhibit good performance as an anode material in LIBs.

Figure 5A shows first galvanostatic charge−discharge cycle for the as-prepared MCNFs as an anode material. The as-prepared MCNFs exhibit large initial irreversible capacity in the first charge−discharge cycle, which is mainly attributable to the electrolyte decomposition on the surface of the carbon material and the formation of a solid electrolyte interface (SEI).[30−37] Low initial coulombic efficiencies have been frequently reported for porous carbonaceous materials with high specific surface areas in LIBs.[6,10,30] Zhou reported an initial coulombic efficiency of 35% for ordered mesoporous carbon CMK-3 with a BET surface area of 1147 m^2 g^{-1},[30] which is much lower than that observed for the as-prepared MCNF (i.e., 51%).

Although a relatively low initial coulombic efficiency is observed for the as-prepared MCNF, the first reversible capacity revealed by the MCNF electrode is very high (ca. 1279 mAh g^{-1}). In addition, from Figure 5B, it is clear that the coulumbic efficiency increases sharply, and after five charge−discharge cycles, the coulombic efficiency reaches over 95%.

The MCNFs exhibit high capacity and good cycle performance. After 100 charge−discharge cycles, the as-prepared MCNF anode material still demonstrates a lithium storage capacity of ca. 1132 mAh g^{-1} (obtained at 100 mA g^{-1} from the delithiation process), corresponding to 89% of the initial reversible capacity, which is much higher than commonly used graphite single-crystal anode with a theoretical specific capacity of 372 mAh g^{-1}.[38−40] Compared with other CNF material without large mesopores in their walls, which has a BET surface area of ca. 220 m^2 g^{-1} and shows a Li storage capacity of 852 mAh g^{-1} @ 30 mA g^{-1},[41] a much higher lithium storage capacity is observed for the as-prepared MCNFs. This mainly
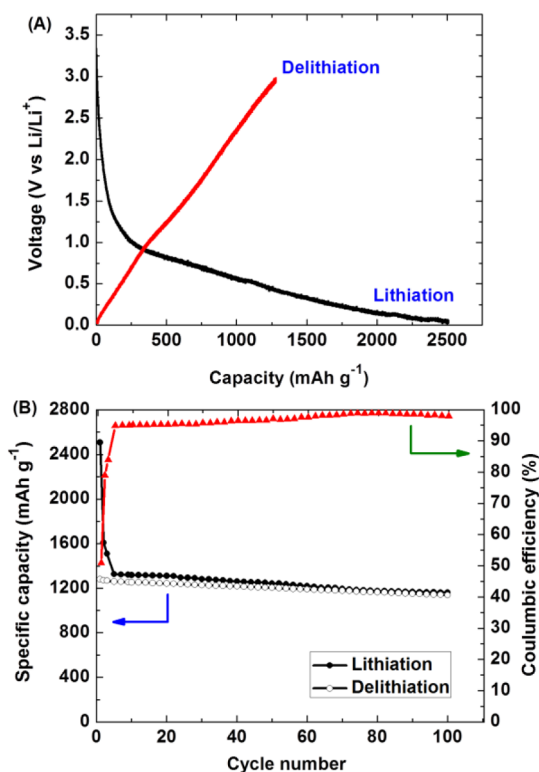
Figure 5. (A) First galvanostatic charge/discharge curve, and (B) specific capacities derived from the lithiation and dethiation processes and coulombic efficiencies shown against the cycle number; all the data were obtained at a charge−discharge rate of 100 mA g^{-1}.

lies in its unique structural characteristics including larger surface area and mesoporous volume for Li storage and, particularly, the hierarchical nanostructure facilitating fast mass transport at high charge/discharge rates.

Compared to OMPC, the MCNFs also show better cycle performance. The specific capacity observed at 100 mA g^{-1} for the as-prepared MCNFs is obviously higher than that (i.e., 799 mAh g^{-1} after 80 cycles) reported for the OMPC, which has a larger specific surface area (i.e., 1120 m^2 g^{-1}).[6] This could be ascribed to higher electrical conductivity of the MCNFs generated from the 1D CNF nanostructure, leading to a low charge-transfer resistance, which is confirmed by the EIS measurements, as shown later in this study.

In addition to high Li storage capacity and excellent cycling performance, the as-prepared MCNF anode material also demonstrates excellent rate capability, as shown in Figure 6. Even at a current density as high as 5000 mA g^{-1}, the electrode maintains a capacity of 880 mAh g^{-1}, corresponding to ca. 69% of the capacity (i.e., 1279 mAh g^{-1}) obtained at 100 mA g^{-1}. It is also interesting to note that, at a discharge rate of 1000 mA g^{-1}, the as-prepared MCNF demonstrates a lithium storage capacity of ca. 1060 mAh g^{-1}, which is much higher than that reported for OMPC (i.e., 758 mAh g^{-1}) and CMK-3 (i.e., 472 mAh g^{-1}).

High lithium storage capacity, good cycling performance, and excellent rate capability observed for the MCNF material are attributable mainly to its unique structure. On one hand, the 1D nanostructure (i.e., nanofiber) facilitates rapid electron transfer along the fiber and brings high electrical conductivity. On the other hand, the hierarchical structure combines macrochannels and mesochannels and micropores together,
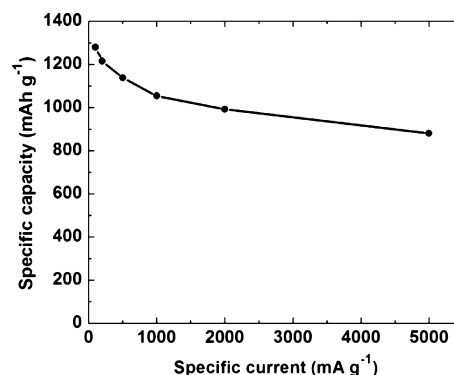
Figure 6. Specific capacities recorded from the delithiation processes at various rates for the as-prepared MCNFs.

which not only favors fast mass transport and good contact between the electrolyte and the electrode, but also generates a highly active interface area during charging−discharging.

To have a better understanding why the as-prepared MCNF outperforms other nanostructured materials, such as the OMPC and CMK-3 reported previously,[6] EIS measurement was conducted for the MCNF. Figure 7 shows a typical Nyquist
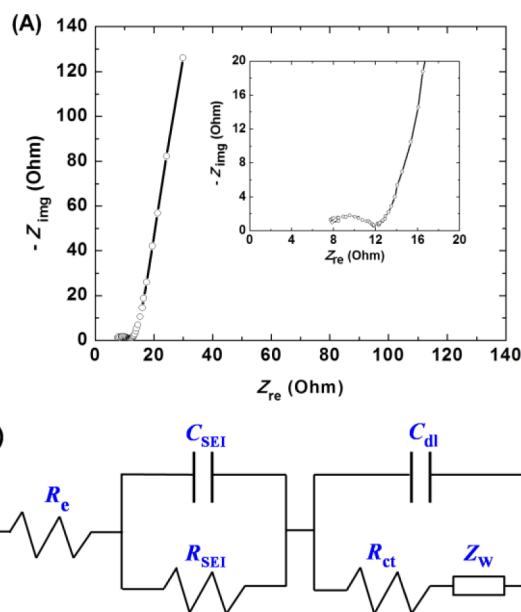
Figure 7. Typical Nyquist plots observed for (A) the as-prepared MCNFs and (B) the derived equivalent circuit.

plot for the electrochemical cell employing the as-prepared MCNF as an active electrode material. A depressed semicircle at high−medium frequency and an inclined line at low frequency were observed for the MCNF. It is well-known that the high−medium semicircle is attributable to the summation of the contact resistance, SEI resistance (R_{SEI}), and charge-transfer resistance (R_{ct}), while the inclined line in the low-frequency region corresponds to typical Warburg behavior, related to the diffusion of lithium within porous carbon materials.[6,42,43] Generally, the contact resistance is small and can be neglected.[44] Based on these assumptions, an equivalent circuit is given in Figure 7B for analysis of the impedance spectrum shown in Figure 7A.

Some kinetic parameters, such as R_{SEI}, R_{ct}, and Warburg impedance (Z_W), are derived and listed in Table 2 by fitting the

Table 2. Kinetic Parameters Derived from the Nyquist Plot for the As-Prepared MCNFs; for the Sake of Comparison, Other Nanostructured Materials (CMK-3 and OMPC) Reported for LIB Applications[6] Are Also Listed Here

sample	R_{SEI} (Ω)	R_{ct} (Ω)	Z_W (Ω)
MCNF	6.9	4.8	5.1
CMK-3	9.2	12.9	13.5
OMPC	7.4	7.6	5.3

impedance spectra to the proposed equivalent circuit, using the software Zview. It is evident that the MCNF material demonstrates a smaller R_{SEI} compared with the OMPC and CMK-3, which could be explained by the comparatively smaller surface area of the MCNF. More interestingly, the MCNF material reveals a R_{ct} value of ca. 4.8 Ω, which is much smaller than that reported for the OMPC (i.e., 7.6 Ω) and CMK-3 (i.e., 12.9 Ω), implying much faster charge transfer in the lithiation and delithiation processes, and facile charge transfer at the electrode/electrolyte interface. It is also interesting to note that the MCNF shows a Z_W of ca. 5.1 Ω, comparable to that reported for the OMPC (i.e., 5.3 Ω), and much smaller than that of CMK-3 (i.e., 13.5 Ω), indicating a much faster lithium transport within the pore network of the MCNF. Compared with the OMPC, much smaller R_{ct} results in higher lithium storage capacity for the MCNF, especially at high charge–discharge rates. When compared with the CMK-3, in addition to much smaller R_{ct} values, much smaller Z_W values also were observed for the MCNF electrode, which is mainly associated with the unique nanostructure of this material, composed of macroscaled channels connected with mesopores of large pore size, facilitating fast mass transport. Actually, fast mass transports have been frequently reported previously for nanostructured materials with hierarchical porosities composed of macropores/mesopores.[45−53] In LIBs, a well-developed 3D network composed mainly of macropores/mesopores is expected to facilitate the mass transport, since electrolyte ions can diffuse easily into and be kept in these channels or pores and behaves similar to that in the bulk electrolyte, and thus bring better ion transport and fast response.[54] Accordingly, an excellent high rate capability can be reached. In addition, for a porous carbon with a hierarchical porosity, the cycling performance can also be improved significantly because a dramatic volume change of the carbon host can be avoided effectively due to the existence of macrochannels and large mesopores, acting as electrolyte buffer reservoirs to reduce the volume change during the cycling.

4. CONCLUSIONS

In this study, a simple and reproducible synthesis strategy was developed to fabricate mesoporous carbon nanofibers (MCNFs) by using porous anodic aluminium oxide (AAO) membrane and colloidal silica Ludox TM-40 as the dual hard templates and phenol resin as the carbon precursor. By using commercial colloidal silica as a co-template, and removing AAO and the silica simultaneously, the synthesis procedures for MCNFs are greatly simplified without the needs of separate preparation of colloidal silica or separate removal of the silica and AAO templates. The as-prepared MCNFs material not only possesses large specific surface area, compared with

conventional carbon nanofibers (CNFs) without large mesopores developed, but also a unique hierarchical nanostructure composed of open macroscaled channels derived from the channels of AAO template, in combination with mesopores of large pore size developed from the removal of colloidal silica and micropores generated from the carbonization of phenol resin. When the as-prepared MCNFs material was explored as an anode in lithium-ion batteries (LIBs), large surface area and mesoporous volume provide a large amount of active sites for lithium storage while low charge transfer resistance originated from one-dimensional (1D) CNFs enable fast electron transfer in the electrode reactions. Particularly, the hierarchical nanostructure composed of highly developed macroporous channels connected with large mesopores facilitates fast mass transport and reduces the volume change during the charge–discharge cycling at high rates. Although a relatively low initial coulombic efficiency is observed for the as-prepared MCNF, the first reversible capacity revealed by the MCNF electrode is still very high (ca. 1279 mAh g^{-1}). Furthermore, the coulombic efficiency increases sharply and reaches over 95% after five charge–discharge cycles. In addition, by the incorporation of TiC[55] or Fe$_3$O$_4$[56] or with an annealing treatment,[56] one can expect an enhancement in the initial coulombic efficiency of the as-prepared MCNF, because of the decreased specific surface area and/or the improved degree of graphitization. Compared with its counterparts, the as-prepared MCNFs anode has demonstrated an ultrahigh lithium storage capacity and excellent cycling performance and rate capability, indicating that the MCNFs material is a very efficient anode candidate for LIB applications.

Through careful control of the size of colloidal silica or other mesopore agents (porogens), MCNFs with varied macropores/mesopores can be produced, which can expand applications of MCNFs to other fields, such as catalyst support for low-temperature fuel cells, adsorbents, and hydrogen storage. Further development of the MCNFs with various macropores/mesopores size for other potential applications is in progress.

■ ASSOCIATED CONTENT

⑤ Supporting Information
Thermogravimetric analysis curve and additional STEM images for the as-prepared MCNFs. This material is available free of charge via the Internet at http://pubs.acs.org.

■ AUTHOR INFORMATION

Corresponding Authors
*E-mail: csc@buaa.edu.cn (S. Zhang).
*E-mail: baizengfang@163.com (B. Fang).

Author Contributions
The manuscript was written through contributions of all authors. All authors have given approval to the final version of the manuscript.

Notes
The authors declare no competing financial interest.

■ ACKNOWLEDGMENTS

■ REFERENCES

(1) Armand, M.; Tarascon, J. *Nature* **2008**, *451*, 652−657.

(2) Liu, N.; Wu, H.; McDowell, M.; Yao, Y.; Wang, C.; Cui, Y. *Nano Lett.* **2012**, *12*, 3315−3321.

(3) Zhang, S.; Du, Z.; Lin, R.; Jiang, T.; Liu, G.; Wu, X.; Weng, D. *Adv. Mater.* **2010**, *22*, 5378−5382.

(4) Kim, M.; Bhattacharjya, D.; Fang, B.; Yang, D.; Bae, T.; Yu, J. *Langmuir* **2013**, *29*, 6754−6761.

(5) Kim, M.; Fang, B.; Kim, J.; Yang, D.; Kim, Y.; Bae, T.; Yu, J. *J. Mater. Chem.* **2011**, *21*, 19362−19367.

(6) Fang, B.; Kim, M.; Kim, J.; Lim, S.; Yu, J. *J. Mater. Chem.* **2010**, *20*, 10253−10259.

(7) Du, Z.; Zhang, S.; Xing, Y.; Wu, X. *J. Power Sources* **2011**, *196*, 9780−9785.

(8) Hu, Y.; Adelhelm, P.; Smarsly, B.; Hore, S.; Antonietti, M.; Maier, J. *Adv. Funct. Mater.* **2007**, *17*, 1873−1878.

(9) Guo, B.; Wang, X.; Fulvio, P.; Chi, M.; Mahurin, S.; Sun, X.; Dai, S. *Adv. Mater.* **2011**, *23*, 4661−4666.

(10) Zhang, S.; Xing, Y.; Jiang, T.; Du, Z.; Li, F.; He, L.; Liu, W. *J. Power Sources* **2011**, *196*, 6915−6919.

(11) Paek, S.; Yoo, E.; Honma, I. *Nano Lett.* **2009**, *9*, 72−75.

(12) Lin, J.; Peng, Z.; Xiang, C.; Ruan, G.; Yan, Z.; Natelson, D.; Tou, J. *ACS Nano* **2013**, *7*, 6001−6006.

(13) Sung, J.; Park, C. *J. Electroanal. Chem.* **2013**, *700*, 12−16.

(14) Boukamp, B.; Lesh, G.; Huggins, R. *J. Electrochem. Soc.* **1981**, *128*, 725−729.

(15) Chan, C.; Peng, H.; Liu, G.; McIlwrath, K.; Zhang, X.; Huggins, R.; Cui, Y. *Nat. Nanotechnol.* **2008**, *3*, 31−35.

(16) Etacheri, V.; Marom, R.; Elazari, R.; Salitra, G.; Aurbach, D. *Energy Environ. Sci.* **2011**, *4*, 3243−3262.

(17) Kim, H.; Seo, M.; Park, M.; Cho, J. *Angew. Chem., Int. Ed.* **2010**, *49*, 2146−2149.

(18) Chen, D.; Mei, X.; Ji, G.; Lu, M.; Xie, J.; Lu, J.; Lee, J. *Angew. Chem., Int. Ed.* **2012**, *51*, 2409−2413.

(19) Ji, L.; Zhang, X. *Nanotechnology* **2009**, *20*, 155705−155711.

(20) Lee, S.; Gallant, B.; Byon, H.; Hammond, P.; Yang, S. *Energy Environ. Sci.* **2011**, *4*, 1972−1985.

(21) Candelaria, S.; Shao, Y.; Zhou, W.; Li, X.; Xiao, J.; Zhang, J.; Wang, Y.; Liu, J.; Li, J.; Cao, G. *Nano Energy* **2012**, *1*, 195−220.

(22) Wang, K.; Birhukovs, P.; Erts, D.; Phelan, R.; Morris, M.; Zhou, H.; Holmes, J. *J. Mater. Chem.* **2009**, *19*, 1331−1338.

(23) Yamaguchi, A.; Uej, F.; Yoda, T.; Uchida, T.; Tanamura, Y.; Yamashita, T.; Teramae, N. *Nat. Mater.* **2004**, *3*, 337−341.

(24) Wu, Y.; Cheng, G.; Katsov, K.; Sides, S.; Wang, J.; Tang, J.; Fredrickson, G.; Moskovits, M.; Stucky, G. *Nat. Mater.* **2004**, *3*, 816−822.

(25) Wang, D.; Kou, R.; Yang, Z.; He, J.; Yang, Z.; Lu, Y.; Bein, T. *Angew. Chem., Int. Ed.* **2006**, *45*, 1134−1138.

(26) Wang, K.; Wei, M.; Morris, M.; Zhou, H.; Holmes, J. *Adv. Mater.* **2007**, *19*, 3016−3020.

(27) Wang, K.; Zhang, W.; Phelan, R.; Morris, M.; Holmes, J. *J. Am. Chem. Soc.* **2007**, *129*, 13388−13389.

(28) Wang, K.; Wang, Y.; Wang, Y.; Hosono, E.; Zhou, H. *J. Phys. Chem. C* **2009**, *113*, 1093−1097.

(29) Fang, B.; Kim, M.; Fan, S.; Kim, J.; Wilkinson, D.; Ko, J.; Yu, J. *J. Mater. Chem.* **2011**, *21*, 8742−8748.

(30) Zhou, H.; Zhu, S.; Hibino, M.; Honma, I.; Ichihara, M. *Adv. Mater.* **2003**, *15*, 2107−2111.

(31) Endo, M.; Kim, C.; Karaki, T.; Nishimura, Y.; Matthews, M.; Brown, S.; Dresselhaus, M. *Carbon* **1999**, *37*, 561−568.

(32) Loebl, A.; Oldham, C.; Devine, C.; Gong, B.; Atanasov, S.; Parsons, G.; Fedkiw, P. *J. Electrochem. Soc.* **2013**, *160*, A1971−A1978.

(33) Kaskhedikar, N.; Maier, J. *Adv. Mater.* **2009**, *21*, 2664−2680.

(34) Casas, C.; Li, W. *J. Power Sources* **2012**, *208*, 74−85.

(35) Zhang, D.; Zhao, Y.; Goodenough, J.; Lu, Y.; Chen, C.; Wang, L.; Liu, J. *Electrochem. Commun.* **2011**, *13*, 125−128.

(36) Yang, S.; Song, H.; Chen, X.; Okotrub, A.; Bulusheva, L. *Electrochim. Acta* **2007**, *52*, 5286−5293.

(37) Oktaviano, H.; Yamada, K.; Waki, K. *J. Mater. Chem.* **2012**, *22*, 25167−25173.

(38) Chen, J. *Materials* **2013**, *6*, 156−183.

(39) Huang, B.; Xue, R.; Li, G.; Huang, Y.; Yan, H.; Chert, L.; Wang, F. *J. Power Sources* **1996**, *58*, 177−181.

(40) Ji, J.; Ji, H.; Zhang, L.; Zhao, X.; Bai, X.; Fan, X.; Zhang, F.; Ruoff, R. *Adv. Mater.* **2013**, *25*, 4673−4677.

(41) Yoon, S.; Park, C.; Yang, H.; Korai, K.; Mochida, I.; Baker, R.; Rodriguez, N. *Carbon* **2004**, *42*, 21−32.

(42) Yang, S.; Feng, X.; Zhi, L.; Cao, Q.; Maier, J.; Müllen, K. *Adv. Mater.* **2010**, *22*, 838−842.

(43) Jamnik, J.; Maier, J. *J. Electrochem. Soc.* **1999**, *146*, 4183−4188.

(44) Park, M.; Kim, K.; Kim, J.; Cho, J. *Adv. Mater.* **2010**, *22*, 415−418.

(45) Fang, B.; Kim, J.; Kim, M.; Yu, J. *Chem. Mater.* **2009**, *21*, 789−796.

(46) Fang, B.; Kim, J.; Kim, M.; Bonakdarpour, A.; Lam, A.; Wilkinson, D.; Yu, J. *J. Mater. Chem.* **2012**, *22*, 19031−19038.

(47) Fang, B.; Bonakdarpour, A.; Kim, M.; Kim, J.; Wilkinson, D.; Yu, J. *Microporous Mesoporous Mater.* **2013**, *182*, 1−7.

(48) Kang, C.; Lahiri, I.; Baskaran, R.; Kim, W.; Sun, Y.; Choi, W. *J. Power Sources* **2012**, *219*, 364−370.

(49) Fang, B.; Kim, J.; Kim, M.; Kim, M.; Yu, J. *Phys. Chem. Chem. Phys.* **2009**, *11*, 1380−1387.

(50) Fang, B.; Kim, J.; Kim, M.; Yu, J. *Acc. Chem. Res.* **2013**, *46*, 1397−1406.

(51) Kim, J.; Fang, B.; Song, M.; Yu, J. *Chem. Mater.* **2012**, *24*, 2256−2264.

(52) Fang, B.; Kim, J.; Kim, M.; Yu, J. *Langmuir* **2008**, *24*, 12068−12072.

(53) Fang, B.; Kim, J.; Lee, C.; Yu, J. *J. Phys. Chem. C* **2008**, *112*, 639−645.

(54) Xu, F.; Cai, R.; Zeng, Q.; Zou, C.; Wu, D.; Li, F.; Lu, X.; Liang, Y.; Fu, R. *J. Mater. Chem.* **2011**, *21*, 1970−1976.

(55) Yao, Y.; Huo, K.; Hu, L.; Liu, N.; Cha, J.; McDowell, M.; Chu, P.; Cui, Y. *ACS Nano* **2011**, *5*, 8346−8351.

(56) Li, G.; Xu, L.; Hao, Q.; Wang, M.; Qian, Y. *RSC Adv.* **2012**, *2*, 284−291.